Article

Ship Detection with Spectral Analysis of Synthetic Aperture Radar: A Comparison of New and Well-Known Algorithms

Armando Marino [1,2]*, Maria J. Sanjuan-Ferrer [3], Irena Hajnsek [1,3] and Kazuo Ouchi [4]

[1] Institute of Environmental Engineering, ETH Zurich, CH-8093 Zurich, Switzerland

[2] The Open University, Department of Engineering and Innovation, Milton Keynes MK7 6AA, UK

[3] Microwaves and Radar Institute, German Aerospace Center (DLR), DE-82234 Wessling, Germany;
E-Mail: Maria.SanjuanFerrer@dlr.de (M.J.S.-F.); irena.hajnsek@dlr.de (I.H.)

[4] Korea Institute of Ocean Science and Technology, Korea Ocean Satellite Center,
Ansan 426-744, Korea; E-Mail: ouchi_sar@yahoo.co.jp

* Author to whom correspondence should be addressed; E-Mail: marino@ifu.baug.ethz.ch;
Tel.: +41-44-633-3404.

Academic Editors: Nicolas Baghdadi and Prasad S. Thenkabail

Abstract: The surveillance of maritime areas with remote sensing is vital for security reasons, as well as for the protection of the environment. Satellite-borne synthetic aperture radar (SAR) offers large-scale surveillance, which is not reliant on solar illumination and is rather independent of weather conditions. The main feature of vessels in SAR images is a higher backscattering compared to the sea background. This peculiarity has led to the development of several ship detectors focused on identifying anomalies in the intensity of SAR images. More recently, different approaches relying on the information kept in the spectrum of a single-look complex (SLC) SAR image were proposed. This paper is focused on two main issues. Firstly, two recently developed sub-look detectors are applied for the first time to ship detection. Secondly, new and well-known ship detection algorithms are compared in order to understand which has the best performance under certain circumstances and if the sub-look analysis improves ship detection. The comparison is done on real SAR data exploiting diversity in frequency and polarization. Specifically, the employed data consist of six RADARSAT-2 fine quad-polacquisitions over the North Sea, five TerraSAR-X HH/VV dual-polarimetric data-takes, also over the North Sea, and one ALOS-PALSAR quad-polarimetric dataset over Tokyo Bay. Simultaneously to the

SAR images, validation data were collected, which include the automatic identification system (AIS) position of ships and wind speeds. The results of the analysis show that the performance of the different sub-look algorithms considered here is strongly dependent on polarization, frequency and resolution. Interestingly, these sub-look detectors are able to outperform the classical SAR intensity detector when the sea state is particularly high, leading to a strong clutter contribution. It was also observed that there are situations where the performance improvement thanks to the sub-look analysis is not so noticeable.

1. Introduction

Monitoring maritime areas with remote sensing is a particularly valuable topic, thanks to the possibility of observing areas that are too large to be properly characterized by sporadic *in situ* visits [1]. In particular, this paper deals with the issue of vessel surveillance or ship detection, which is a crucial topic for several reasons, including security and protection of the environment. An example of the latter is the monitoring of no-navigation zones, such as natural parks. Additionally, illegal fishery could be detected by surveilling the protected areas with remote sensing. In this context, synthetic aperture radar (SAR) [2] has the advantage of providing high-resolution images, which is extremely valuable for the detection of small vessels (a few tens of meters long, as can be the case for fishing boats) [3].

The aim of this paper is to test a series of ship detectors based on spectral analysis of SAR images to evaluate the situations where it is beneficial to use such methodologies compared to more traditional ways of processing data. This work has two main novelties:

1. Two recently proposed algorithms aimed at detecting coherent scatterers for interferometry and tracking methodologies are tested for the first time for ship detection. These are the generalized likelihood ratio test (GLRT) of sub-look images [4,5] and the sub-look entropy [6].
2. The paper proposes the first comparison of four sub-look detectors exploiting a large dataset composed of TerraSAR-X, RADARSAT-2 and ALOS-PALSAR (with diversity in frequency, polarization channels and incidence angles).

The motivation for such a comparison follows the observation that spectral analysis was shown to help to detect ships when their contrast with the sea is very low (i.e., the ship is not easily visible in the intensity images) [7,8]. It is the aim of this work to understand if such a capability is repeatable on a larger dataset and how the different sub-look detectors compare with one another.

It has been observed that the main feature of ships in SAR images is a bright backscattering. This can be explained by the presence of several metallic structures and corners. On the other hand, the sea behaves as a rough surface. Specifically, the Bragg model was proven to be a reliable scattering model for the sea in ordinary observational conditions [9]. Important factors influencing the Bragg backscattering are: surface roughness, incidence angle and frequency [9–14]. The backscattering signal from the sea is generally lower than the one from vessels, since a large part of the electromagnetic radiation impinging

on the sea is scattered in the mirror direction. For this reason, ships often appear as bright spots in SAR intensity images. This peculiarity has led to the development of several algorithms aimed at detecting bright points on a darker background [3,15–19,22–30]. The backscattering from the sea is strongly influenced by the sea state, and in some situations, it can be extraordinarily bright, covering the return from small vessels. This issue is especially true for frequencies higher than 5 GHz (C-band) and steeper incidence angles (e.g., lower than 25 degrees). Additionally, there are other maritime features, such as braking or rogue waves, that can originate high backscattering. Such bright areas may lead to false alarms in detectors based on intensity only. In order to solve for this problem, statistical tests on the local clutter intensity can be devised to adjust the threshold according to sea clutter. A commonly-used methodology tries to keep constant the probability of false alarm (P_f) and, therefore, is called the constant false alarm rate (CFAR) [31]. This statistical test is able to mitigate the occurrence of false alarms; however, the results are strongly dependent on the dimensions of local windows, and the estimation of the distribution parameters can lead to greatly biased results (e.g., estimating the equivalent number of looks).

An alternative way of tackling the problem of a bright sea clutter is to devise a methodology capable of reducing the clutter while preserving as much as possible the vessel return. This procedure would therefore increase the vessel-over-sea contrast. The aim of this paper is to analyze methodologies that attempt to provide such increased contrast exploiting the information kept in the image spectrum (i.e., discrete Fourier transform of the complex image). The spectral analysis of SAR data mostly consists of extracting the spectrum and analyzing portions of it, here defined as the sub-spectrum. The image that is obtained executing the anti-transformation of a sub-spectrum is referred in the following as a sub-look or sub-image. These operations can be efficiently done employing an FFT (fast Fourier transform) algorithm [32]. Furthermore, such approaches were revealed to be beneficial to detect point-like targets, that is coherent targets [6,33,34].

In the context of ship detection with sub-images, different methodologies can be devised [7,8,35], but they often share a common principle. The latter is that the sea complex backscattering (the one considering single-look complex (SLC) images) can be modeled as the one from a distributed target with fully-developed speckle [36]. Then, it can be demonstrated that two non-overlapping sub-spectra of the sea spectrum (i.e., an area presenting only homogeneous sea clutter) are completely uncorrelated [34]. This is the direct consequence of the statistical nature of the sea complex pixels (i.e., the two portions of the spectrum represent completely different speckle patterns). Please note, this property is only fulfilled for the spectrum of complex images; if intensity images are considered, then the spectra will not have this property anymore. For this reason, SLC images are necessary, and the processing illustrated in the following is different from the extraction of wave spectra [9,11], which is performed on intensity images.

If a point target with very large backscattering is considered, its spatial behavior can be modeled as a Dirac delta [32], which means that its spectrum is constant. As a consequence, different portions of its spectrum are perfectly correlated. Clearly, these are only ideal situations, which are not completely fulfilled in real scenarios. Nevertheless, these concepts can be used as guidelines to devise signal processing methodologies aimed at enhancing the contrast between vessels and sea clutter and singling out point targets.

The sub-look detectors presented in the next section will be compared with two detectors that do not perform any sub-look analysis. They are based on the intensity of the backscattering considering SLC

(i.e., without filtering) or multi-look (i.e., boxcar filtering) images [3]. These are well-known approaches that do not need phase information. The comparison would help with understanding the usefulness of acquiring SLC images instead of detected images (i.e., images without phase).

Finally, diversity in polarization will be tested, as well. Polarimetric acquisitions are obtained changing the polarization of the antennas used in transmission and reception, and it is aimed at acquiring the scattering (or Sinclair) matrix. This matrix is composed of the polarization channels HH, VV, HV and VH, where H stands for linear horizontal and V for linear vertical, and the repeated letter stands for the transmitted-received combination.

2. Spectral Analysis of SAR Data

In this section, the basic processing steps to extract sub-images from a SAR spectrum are illustrated. By definition, an image formed using just a portion of the full available system bandwidth is called a sub-look image or simply a sub-image. Consequently, a sub-look image has a resolution proportionally lower than the resolution of the original image and a different central frequency. The resolution loss is proportional to the ratio between the reduced and full bandwidth sizes. More than two sub-look images can theoretically be created, therefore allowing a partial overlap between the sub-look bandwidths. Moreover, such sub-images can be generated in the range direction, azimuth direction or both at the same time, and the process can be carried out in the time or frequency domain. The physical interpretation of the processing in the range and azimuth is different. Therefore, it is interesting to consider this in order to have a better understanding of the feasible methodologies.

- Sub-looking in the range: In this case, the stability of the targets is tested with respect to variations of frequency. This is due to the fact that, after removal of windowing, the spectrum pixels in range contain the backscattering values when the frequency of the chirp is varied. An ideal point target and (generally) corner reflectors have a response that stays coherent when changing the frequency slightly. By definition, this is the reason why such targets can be focused as single points in an SAR image [34,37].

- Sub-looking in the azimuth (or Doppler): The stability of targets is now tested when they are observed by different angles in the azimuth footprint of the SAR acquisition (i.e., looking fore or aft). Again, a theoretical point target is perfectly isotropic, while static corners mostly stay coherent (even though their amplitude can change significantly along the synthetic antenna). Unfortunately, the Doppler analysis becomes more complicated when the targets are not stationary. Targets that move along the range direction have a different Doppler history compared with static targets. This circumstance has two main effects: firstly, the zero Doppler will be located in a different position, translating the target along the azimuth direction; secondly, the focusing cannot be done optimally (since the Doppler history does not match the reference one), which means that the target will present smearing (i.e., de-focusing). In the framework of ship detection, smearing leads to not having a point target anymore, and therefore, a coherent detector may fail. As a final remark, the Doppler analysis may be performed keeping in mind the possibility of miss detections due to vessel movements [37,38].

In principle, sub-look images should be obtained by filtering the raw data. However, especially for space-borne sensors, raw data are not always provided due to the data policies of space agencies. On the other hand, standard image pre-processors can be considered linear and phase preserving to a large extent, implying that the whole information in the frequency domain is preserved after focusing, apart from the windowing operation necessary to reduce sidelobes. Accordingly, the sub-look images can be generated directly from focused images by calculating the Fourier transform of the image (in the range or azimuth), removing the windowing and selecting a portion of the full spectrum, i.e., by multiplying such a spectrum by a rectangular weighting function and computing its inverse Fourier transform [4,5]. A diagram summarizing the main steps of the sub-looking process in the range direction is depicted in Figure 1.
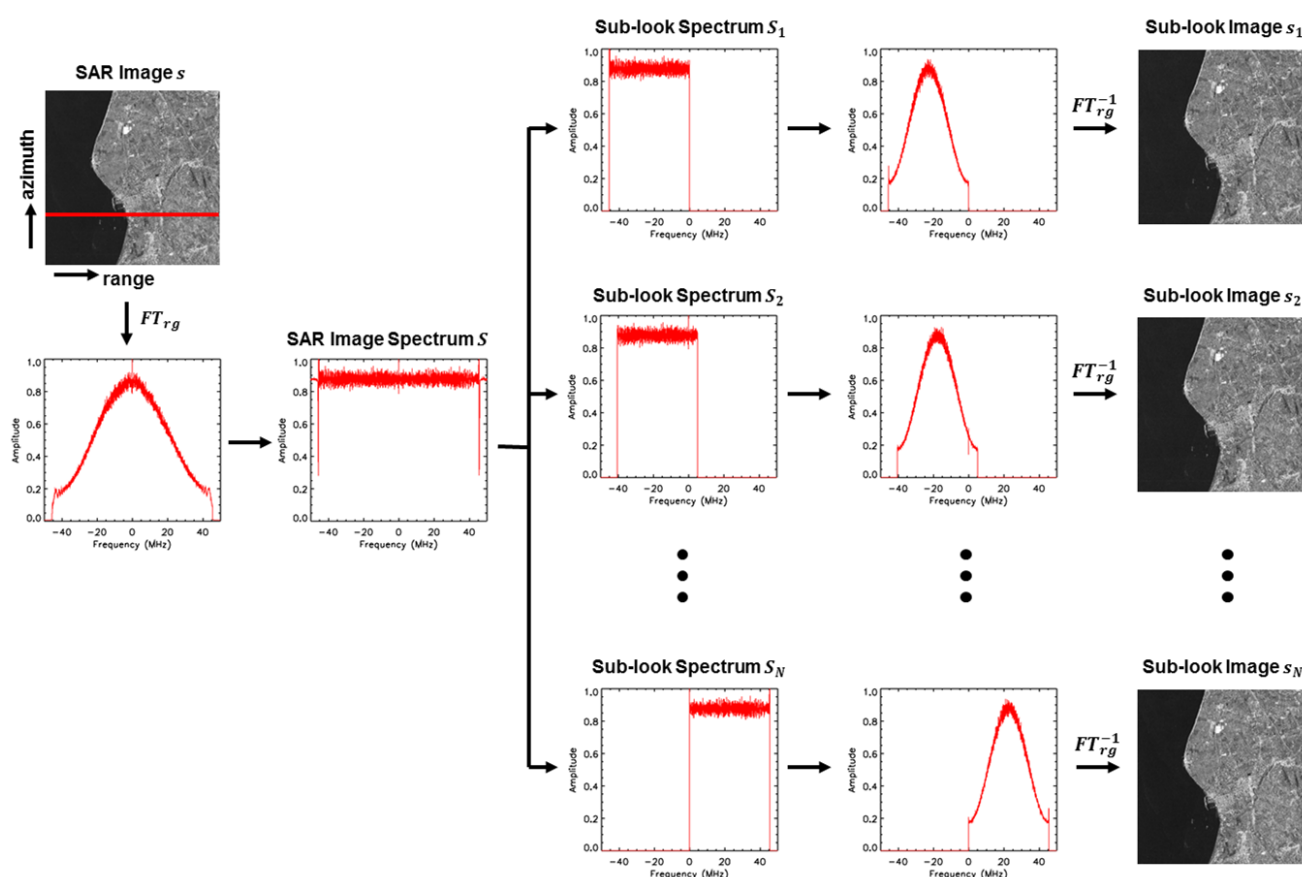

Figure 1. Flow chart of sub-look extraction.

It is important to remark that all of this process can be done without using any information regarding the selected sensor. For instance, the range window or azimuth antenna pattern can be estimated by calculating the corresponding medium spectrum in the selected direction (range or azimuth, respectively).

Once the sub-images have been generated, they will be combined together according to some procedure, as explained in the successive Section 3. In the following, s indicates the initial image, while the sub-image is referred to as s_i, with i an index identifying the corresponding i-th portion of the spectrum S_i.

3. Target Detectors with Spectral Analysis

3.1. Sub-Look Coherence

The sub-look coherence was the first ship detector exploiting sub-images [7,8]. It splits the full spectrum into two non-overlapping sub-spectra, often along the azimuth direction. After the anti-transformation, the sub-images are used to calculate the coherence between them with a moving window:

$$\gamma = \frac{|\langle s_1 \cdot s_2^{*T} \rangle|}{\sqrt{\langle s_1 \cdot s_1^{*T} \rangle \langle s_2 \cdot s_2^{*T} \rangle}} \tag{1}$$

where $*^T$ stands for the conjugate transpose and $\langle \rangle$ defines a spatial average (e.g., a boxcar filter).

3.2. Sub-Look Cross-Correlation

A methodology based on the same principle as the sub-look coherence has been presented in [35,39]. However, there are two major differences with the previous algorithm. Firstly, the cross-correlation between sub-images is not normalized:

$$\rho = |\langle s_1 \cdot s_2^{*T} \rangle| \tag{2}$$

Secondly, the sub-images are obtained by extracting portions that can overlap in the spectral domain, making possible also the detection of vessels that are not robustly stable in the transformed domain. Because of the partial overlap, the sea contribution might not be rejected as strongly as before. Nevertheless, it has been shown in [35] that the contrast of a sea vessel for ρ can be improved by overlapping spectrum portions.

3.3. Sub-Look Entropy

The coherence is a useful operator for expressing the correlation between two images. However, when more images are considered, several coherences should be estimated. Alternatively, the covariance matrix of the stack of sub-images can be estimated, and the entropy of the eigenvalues can be derived. If the entropy is zero (i.e., one strongly dominant eigenvalue), then all of the sub-images represent the same target or, in other words, the target in the averaging window is completely stable over the different spectral portions [6]. Denoting by $\underline{x}$ the vector of sub-images (i.e., $\underline{x} = [x_1, ..., x_n]^T$, where n sub-images are considered), the covariance matrix can be calculated as $[X] = \langle \underline{x} \cdot \underline{x}^{*T} \rangle$. Being λ_i the *i*-th eigenvalue obtained by the diagonalization of $[X]$, the entropy is calculated as:

$$H = -\sum_{i=1}^{n} p_i \log_n p_i \tag{3}$$

where $p_i = \frac{\lambda_i}{Trace([X])}$ [6]. The sub-look entropy detector is tested here for the first time with the objective of ship detection.

3.4. GLRT

Recently, a methodology for detecting coherent targets based on the generalized likelihood ratio test (GLRT) was proposed [4,33]. The algorithm sets a test based on a statistical model for sea clutter and vessels. The analytical expression of the GLRT is:

$$L_G = \frac{|\underline{a}^{*T}M^{-1}\underline{x}|^2}{\left(\underline{a}^{*T}M^{-1}\underline{a}\right)\left(\underline{x}^{*T}M^{-1}\underline{x}\right)} \tag{4}$$

where $\underline{a}$ is the vector with the location of the scatterer in the resolution cell (in this test, the scatterers are assumed at the center of the resolution cell), $\underline{x}$ is the vector with the complex amplitudes of the pixel under test along the sub-looks and M is the theoretical normalized covariance matrix of the clutter, which depends on the number of sub-images n and the ratio between the total and the sub-look spectra. The complete procedure to calculate M can be found in [4,33]. The bilinear form L_G is one for perfectly coherent (i.e., spectrally stable) targets. The formulation of the GLRT detector Equation 4 has been derived under the hypothesis of Gaussian clutter. However, its optimality can be extended to the compound-Gaussian clutter distribution family if a large number of sub-looks n is used, as an intrinsic property of the probability density function of a compound-Gaussian vector [20]. In our framework of vessel detection, the sea clutter is frequently modeled in the radar literature as *K*-distributed, which is still a compound-Gaussian distribution. Nevertheless, in the case that the clutter is not compound-Gaussian distributed, the GLRT detector Equation 4 can be still applied, but its performance should be verified *a posteriori* with real data, as done in this paper. The GLRT detector is firstly tested for ship detection, making use of $n = 30$ (equidistant) overlapping sub-look images extracted from the full spectrum, each of them with a sub-look bandwidth of 50%. That corresponds to a spectrum overlap between sub-looks of approximately 96%. However, such an overlap is known and included in the matrix M, and the GLRT detector uses this correlation information for whitening the clutter before the detection is performed. Notice that the numerator of Equation 4 corresponds to the power output by a matched filter of the data vector $\underline{x}$ after whitening transformation of the clutter.

4. Methodology Employed for the Algorithm Comparison

4.1. Receiver Operating Characteristic Curves

In this section, the procedure employed for testing and comparing the algorithms is discussed in detail. The selection of thresholds is a particularly crucial step for a fair detector comparison. If the probability density functions (pdf) of the outputs given by each algorithm do not fit known pdfs well, a comparison based on CFAR thresholds may return misleading results. In fact, the obtained detection masks will be strongly dependent on the specific pdf selected, and therefore, such a comparison may reveal more the fitting of the selected pdfs than the quality of the detector itself. In order to avoid this problem, an analysis independent of the specific threshold can be executed. In this paper, the receiver operating characteristic (ROC) curves are employed instead. An ROC is obtained by plotting the probability of a false alarm P_f over the probability of detection P_d, while the threshold is varied. In other words, an ROC reveals the P_d that can be obtained with a fixed P_f. In the case of a (perfect) CFAR algorithm, ROC

curves can be used to aid the selection of P_f. Lastly, good detectors are closer to the upper left corner on the ROC plane (i.e., $P_d \approx 1$ and $P_f \approx 0$).

The ROC curves shown here for the different detectors and sensors have been computed by executing the same software procedures. In particular, P_d and P_f are computed by varying the threshold between a minimum and a maximum value, depending on the histogram of the detector output and using logarithmic scales when the dynamic range is particularly large (e.g., the intensity detector).

4.1.1. Computation of P_d

P_d is calculated by counting the number of detected vessels over the total number of vessels present in the selected dataset. Specifically, each vessel is counted as one, and the wide-spread approach of considering each pixel of the vessel as an independent count is not employed here. The motivation for this is related to the fact that neighbor pixels in SAR images are not independent, and bright pixels may have a spreading function that largely overlays immediate neighbors. Furthermore, some of the tested detectors execute spatial averaging, which adds extra correlation between neighbor pixels.

Practically, an area around what is identified as the center of the vessel is considered as the vessel region of interest (ROI). The pixel size of ROIs depends on the sensor resolution. If at least one pixel is detected inside the ROI, the vessel is called detected. The estimation of P_d has a quantization error equal to the inverse of the total number of vessels in the dataset. More details on the quantization error are provided in the section dedicated to the presentation of the datasets.

4.1.2. Computation of P_f

P_f is estimated by selecting sea regions clear from vessels, land or evident image artifacts (e.g., azimuth ambiguities) and counting the number of detected pixels over the total number of pixels of the region. In order to avoid some pixels from large vessels producing false alarms, guard areas around ships are used, and such pixels are excluded from the false alarm analysis. Further information regarding the number of pixels in each dataset is provided in the following.

4.2. Detector Parameters

Each of the detectors considered here requires the setting of their algorithm parameters. Two main categories of parameters can be identified:

- The first one is related to the process of splitting the image spectrum: the number of sub-images and their overlap in frequency.
- The second one corresponds to the size of windows for eventual boxcar filtering. In this work, the window size of the boxcar filter is never squared, since the resolution in the ground range and azimuth are not the same. In addition, it is assumed that vessels do not have preferential orientations in the horizontal plane (direction of travel).

Tables 1 and 2 summarize the nominal settings used for each detector. However, some parameters will be varied during the analysis in order to understand their effect in the detection performance.

As a final remark, it is important to notice that the selection of detection parameters is strongly dependent on the employed sensor. Consequently, the parameters that will not be varied are the ones that either were suggested in the literature or that provide the best performance. In general, the key factors in this study are resolution, frequency and mean size of the vessel of interest.

Table 1. Parameters used for sub-look generation. GLRT, generalized likelihood ratio test.

Detector	♮ Sub-Images	Band Overlap
GLRT	30	96%
Entropy	3	50%
Correlation	2	0% or 50%
Coherence	2	0%
Intensity	None	None

Table 2. Parameters used for boxcar filtering.

Detector	RADARSAT-2 (Range × Azimuth) Pixels	TerraSAR-X (Range × Azimuth) Pixels	ALOS-PALSAR (Range × Azimuth) Pixels
GLRT	None	None	None
Entropy	(5×9) or (3×5)	(13×5) or (7×3)	(3×15) or (5×25)
Correlation	(5×9) or (3×5)	(13×5) or (7×3)	(3×15) or (5×25)
Coherence	(5×9) or (3×5)	(13×5) or (7×3)	(3×15) or (5×25)
Intensity	None or (5×9) or (3×5)	None or (13×5) or (7×3)	None or (3×15) or (5×25)

5. Experimental Data

This section presents all the datasets employed for the detector comparison. Such datasets try to cover several conditions with respect to frequency, sea state, polarization channels and incidence angles. In total, 12 acquisitions, including RADARSAT-2, TerraSAR-X and ALOS PALSAR data, are considered.

5.1. RADARSAT-2

Six fine quad-polarimetric images were acquired during winter 2013/2014 in the North Sea and Kattegat. These data were collected under the SOARproject EI-5145. Figure 2 shows the locations of the different images as polygons on Google Earth.

The central frequency is the C-band (5.4 GHz), while the chirp bandwidth is 30 MHz. Several antenna beams (i.e., incidence angles) were considered in order to capture different observation conditions. All of the scenes are in single-look complex (SLC) format, covering approximately 25×25 km^2, with a slant range resolution of 5.2 m and an azimuth resolution of 7.6 m. The image noise equivalent sigma zero (NESZ) is around -36 dB. Further details about the acquisitions are provided in Table 3.

One objective of the SOAR project EI-5145 is to test ship detectors under severe weather conditions. In order to amplify the effects of strong sea clutter, large incidence angles (higher than $35°$) were avoided. One of the acquisitions 3 December 2013 also includes a very steep incidence angle (e.g., $\sim 21.5°$). With

the purpose of increasing the probability of observing rough sea conditions, the test areas were selected with relatively high latitudes and during the winter season. On the other hand, care was taken to select areas with large traffic of vessels. The scenes in the North Sea are close to the harbors of Rotterdam and Amsterdam, while the ones in the Kattegat are around Anholt Island, along the shipping route from the North Sea to the Baltic Sea.

Figure 2. Locations (red polygons) of the six RADARSAT-2 fine quad-polacquisitions used in the comparison: Google Earth.

Table 3. Details on fine quad-pol RADARSAT2 data. Time is in UTC. AIS, automatic identification system.

Date (Time)	Location	Beam	Incidence Angle	Ground Range Res.	Wind Speed (m/s)	Ships with AIS
29 November 2013 (17:30)	North Sea	FQ12	$\sim 32°$	10.0 m to 9.5 m	16.5 (NW)	12
3 December 2013 (05:48)	Kattegat	FQ3	$\sim 21.5°$	14.6 m to 13.4 m	10.8 (SW)	6
23 December 2013 (17:30)	North Sea	FQ13	$\sim 34°$	9.7 m to 9.3 m	18.5 (S)	13
10 December 2013 (05:43)	Kattegat	FQ6	$\sim 25°$	13.1 m to 12.2 m	6.7 (SW)	9
16 January 2014 (17:30)	North Sea	FQ15	$\sim 35°$	9.2 m to 8.8 m	9.8 (S)	9
9 February 2014 (17:30)	North Sea	FQ15	$\sim 35°$	9.2 m to 8.8 m	18 (SW)	20

In total, 69 validated ships were observed with a variety of dimensions (ranging between 30 m to 200 m in length) and typology (e.g., fishing boats, cargo boats, *etc*). Since a finite number of vessels is exploited, there is a minimum change of probability that can be estimated (or a minimum probability that can be estimated). This minimum difference will be refereed in the following as a quantization error. Such a number of vessels translates into a quantization error for the estimation of P_d equal to 0.015.

5.2. TerraSAR-X

The TerraSAR-X data were acquired during winter 2012/2013. As for the previous dataset, the planning of acquisitions was made trying to maximize the probability of obtaining rough sea conditions. Several locations in the North Sea (Aberdeen), the Channel Sea (Portsmouth), Kattegat (Goteborg) and the Baltic Sea (around Bornholm Island) were selected, close to important harbors or shipping routes. Figure 3 presents the test areas as polygons on Google Earth. For all images, the azimuth resolution is 6.7 m, while the slant range resolution is 1.1 m (i.e., the chirp bandwidth is $\sim$ 150 MHz). The swath width is 15 km, and the length of the strip is generally 150 km. The NESZ is around -21 dB. For this dataset, two polarimetric channels HH/VV were considered. Table 4 summarizes further details regarding the acquisitions.

Figure 3. Location of the five TerraSAR-X dual-pol HH/VV acquisitions used in the comparison. The red polygons indicate the locations: Google Earth.

Table 4. Details on HH/VV TerraSAR-X images exploited in the comparison. Time is in UTC.

Date (Time)	Location	Beam	Incidence Angle	Ground Range Res.	Wind Speed (m/s)	Ships with AIS
03 December 2012 (06:33)	Aberdeen	stripFar_008	$\sim 33.5°$	2.1 m	6.7 (SE)	16
11 December 2012 (16:36)	Baltic Sea	stripFar_005	$\sim 27°$	2.6 m	11.8 (N)	8
05 December 2013 (16:45)	Goteborg	stripFar_006	$\sim 29°$	2.4 m	Not Recorded	6
18 December 2013 (17:45)	Portsmouth	stripNear_007	$\sim 30°$	2.3 m	Not Recorded	7
29 December 2013 (17:45)	Portsmouth	stripNear_007	$\sim 30°$	2.3 m	Not Recorded	12

The analyzed images contain 49 validated vessels, which translates into a quantization error in estimating P_d of 0.02.

5.3. ALOS-POLSAR

Finally, a quad-polarimetric dataset over the Tokyo Bay area (Japan) is considered. The area is renowned to have a large amount of traffic of vessels. The acquisition was performed on 9 October 2008 (10 : 19 a.m. local time). The resolution in the ground range is about 27 m, while in the azimuth, it is about 4.9 m. The incidence angle is about 24°, and the average intensity of sea clutter (outside the Bay) in the VV polarization is around $\sigma^0 = -2.5$ dB. Additionally, the slant range resolution is 11.1 m, while the pixel spacing in the slant range is 9.4 m. The pixel spacing in the azimuth is 3.6 m. A Google Earth image of the area of interest by the analysis is displayed in Figure 4.
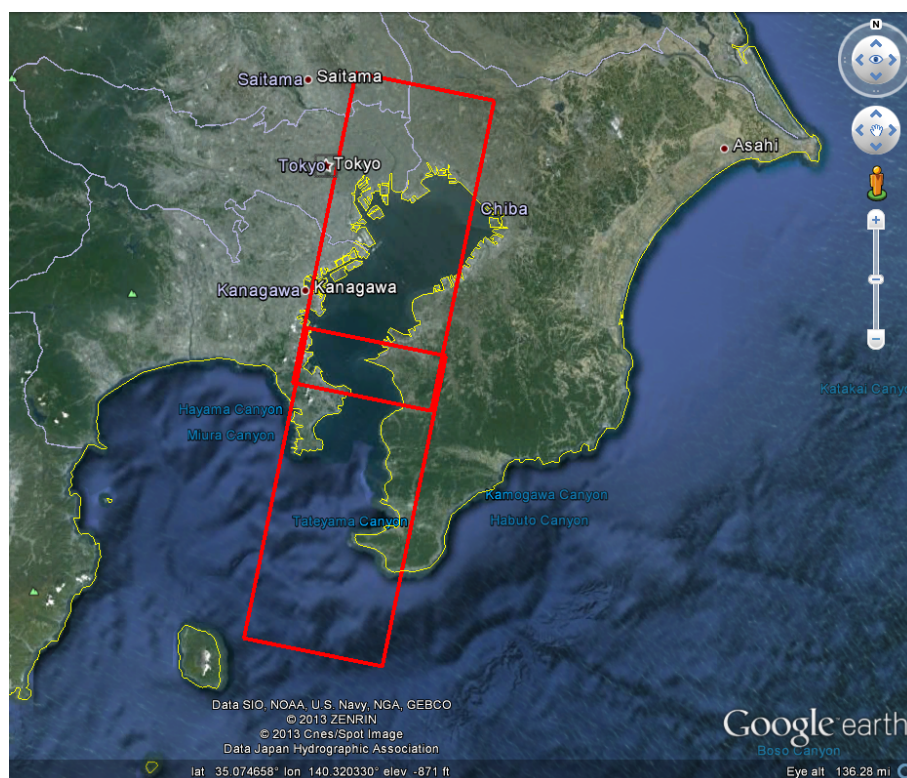
Figure 4. Location (red polygons) of the quad-polarimetric ALOS-PALSAR data. Google Earth.

During the acquisition, a ground survey was carried out combining different instruments. A video of vessels crossing a portion of the Tokyo Bay was captured, in cooperation with an X-band ground-based radar. Both the video camera and radar were located on the top of the National Defense Academy (NDA) building (at the west shore of the bay) at an altitude of approximately 100 m above the sea level. The survey indicated that 38 vessels were present in the test area, but only 22 of them can be identified after a visual inspection. Moreover, it is possible to recognize other vessels as bright points with wakes. This leads to a total of 48 vessels. Finally, some areas were covered by sea weed farms (laver), which are constituted by wooden platforms. Five of these platforms were also included in the analysis in order to test the detectors with very challenging targets. More details are provided in the following. Regarding the sea state, we have information inside the bay where the significant wave height is 0.7 m in the 190° direction from north. The period is 1.8 s, and the wind speed is 11.2 m/s (strong breeze: six in the Beaufort scale) in the 20° direction.

6. Detectors Comparison

6.1. Comparison with RADARSAT-2 Data

As previously explained, the spectral analysis can be done in the range or azimuth direction. Hereafter, these two approaches are treated in separate sections. In addition, some of the detectors need to perform averaging in order to estimate their output, as already mentioned. In order to ease the readability of the curves, the results for different window sizes are presented in different plots. On the other hand, detectors that do not need averaging (i.e., GLRT and SLC intensity) will be plotted in each figure to aid the comparison. Finally, the ROC curves for each polarization channel are also considered separately.

6.1.1. Sub-Look Processing in the Range

The first test considers a boxcar window of (5×9) pixels. Figure 5 presents the obtained ROC curves for the three polarization channels, HH, VV, HV. Notice that it is not necessary to show the VH ROC, since it is equal to the one of HV, except for thermal noise.
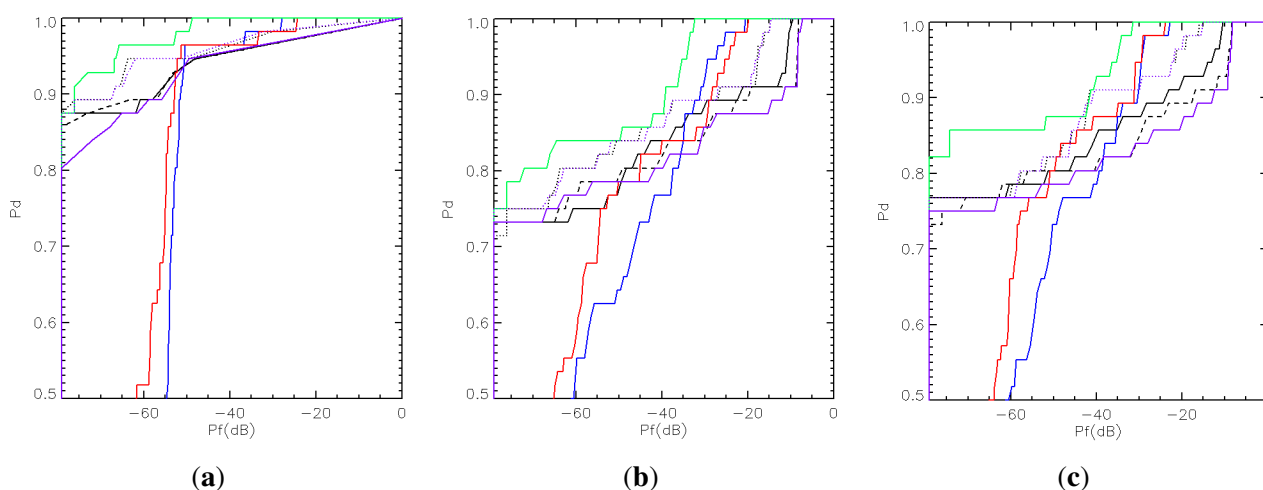
Figure 5. Detector ROC curves for sub-look analysis in the range direction. RADARSAT-2 fine quad-pol data. Boxcar filter: 5×9 (range $\times$ azimuth) pixels. (**a**) HV channel; (**b**) HH channel; (**c**) VV channel. Vessels analyzed: 69; pixels used for P_f: $\sim 10^{-7}$. Black: sub-look correlation (solid: filtered with no overlap; dashed: filtered 30% overlap); blue: sub-look coherence; green: GLRT; violet: intensity (dotted: no average; solid: averaged); red: sub-look entropy.

Before we start comparing algorithms, it is interesting to observe the behavior of the detectors for different polarimetric channels. The cross-polarization (HV) channel is able to provide better ROC curves compared with the co-polarization ones (HH and VV). This outcome has been also observed by other researchers [3,21,40,41]. According to the Bragg model, sea clutter has a very low (or even null) backscattering in the cross-channel, leading in many circumstances to an increased contrast. Several works deal with exploiting polarimetric information to improve the detection performance [42–44,46–48], but such a methodology is out of scope of this work, which is focused on understanding the potential of sub-look analysis.

Regarding the comparison of the different detectors, it has been obtained that the GLRT provides the best detection performance. It is necessary to remark that in the following, the comparisons are mostly done considering rather high values of P_d (e.g., greater than 0.8), since these are the most interesting operation scenarios. A common requirement in ship detection is to have $P_f < 10^{-4}$ (one over 10,000 pixels). Interestingly, by exploiting the HV channel, the GLRT can meet this requirement on this dataset with a unitary P_d (i.e., all vessels detected), while P_d is lowered to around 0.85 for the co-polarization channels. The second and third best performances are the ones provided by the sub-look coherence and the sub-look entropy detectors, respectively. Concerning the sub-look correlation method, two versions have been tested in this paper following the observation that a different overlap of sub-spectra can provide different results [35]. For this reason, one version (solid black line) considers non overlapping sub-spectra, and the other (black dashed line) exploits sub-spectra with 30% overlap.

As already indicated, the sub-look algorithms are compared with two detectors based on the intensity and considering SLC (without filtering) or multi-look (boxcar filtering) images [3,49]. It is interesting to note that the intensity detector on the cross-polarization shows large performance loss only if compared with the GLRT. This is an indicator that, if the cross channel is available, the gain of acquiring SLC instead of detected images would be clearly noticeable only if the GLRT is exploited. This situation is not true for the co-polarization channel, where the sub-look process provides benefits for all of the sub-look detectors with the exception of the cross-correlation method.

The intensity detector shows that the performance improves if the filtering is not performed (dotted violet compared with solid violet). A possible explanation for this phenomenon can be that some of the vessels considered in the analysis are small, and as a consequence, the resolution becomes a crucial parameter (even more important than speckle reduction). In order to investigate this situation, the size of the used boxcar is reduced to (3×5) pixels, and the obtained results are displayed in Figure 6. As can be observed, the ROCs of the detectors employing filtering (i.e., coherence, entropy and correlation) improve slightly.

6.1.2. Sub-Look Processing in the Azimuth

The second test corresponds to the analysis along the azimuth direction. The results of the detector comparison exploiting a (3×5) boxcar is presented in Figure 7. At first glance, it seems that the ROCs are similar to the ones obtained for the range analysis. However, it can be noticed that the performance is slightly reduced for all of the sub-look detectors. Such a loss could be explained by the effects of moving vessels. Since the performance worsening is not very large, some corrections to the smearing of moving vessels (i.e., better focusing of vessels exploiting the correct Doppler) may lead to the same performance using azimuth or range analysis.

The analysis of different window sizes for the azimuth is not presented here for the sake of brevity, but the results are equivalent to the ones obtained in the range.
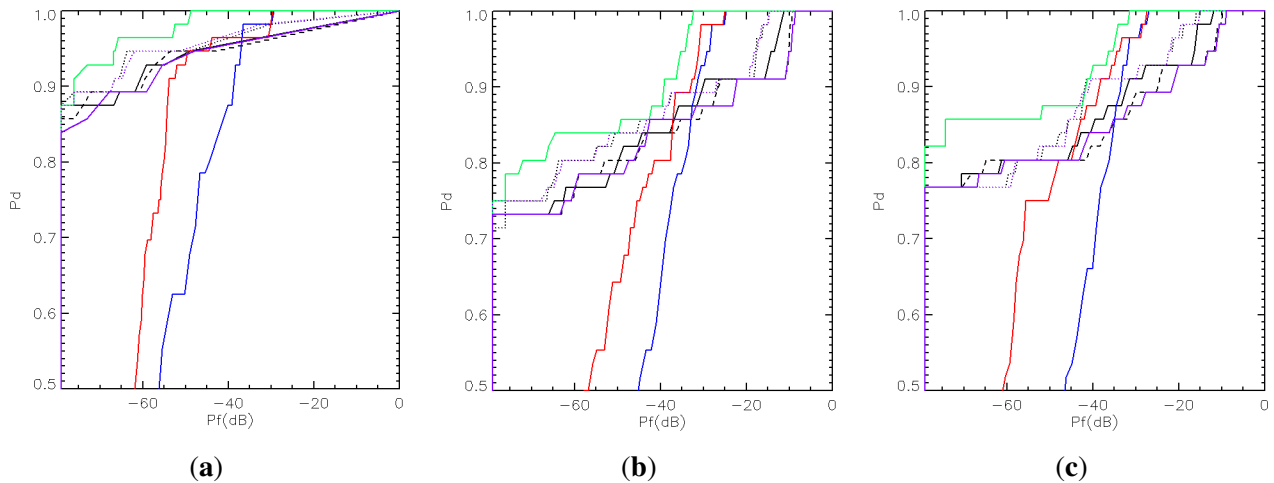
Figure 6. Detector ROC curves for sub-look analysis in the range direction. RADARSAT-2 fine quad-pol data. Boxcar filter: 3×5 (range $\times$ azimuth) pixels. (**a**) HV channel; (**b**) HH channel; (**c**) VV channel. Vessels analyzed: 69; pixels used for P_f: $\sim 10^{-7}$. Black: sub-look correlation (solid: filtered with no overlap; dashed: filtered 30% overlap); blue: sub-look coherence; green: GLRT; violet: intensity (dotted: no average; solid: averaged); red: sub-look entropy.
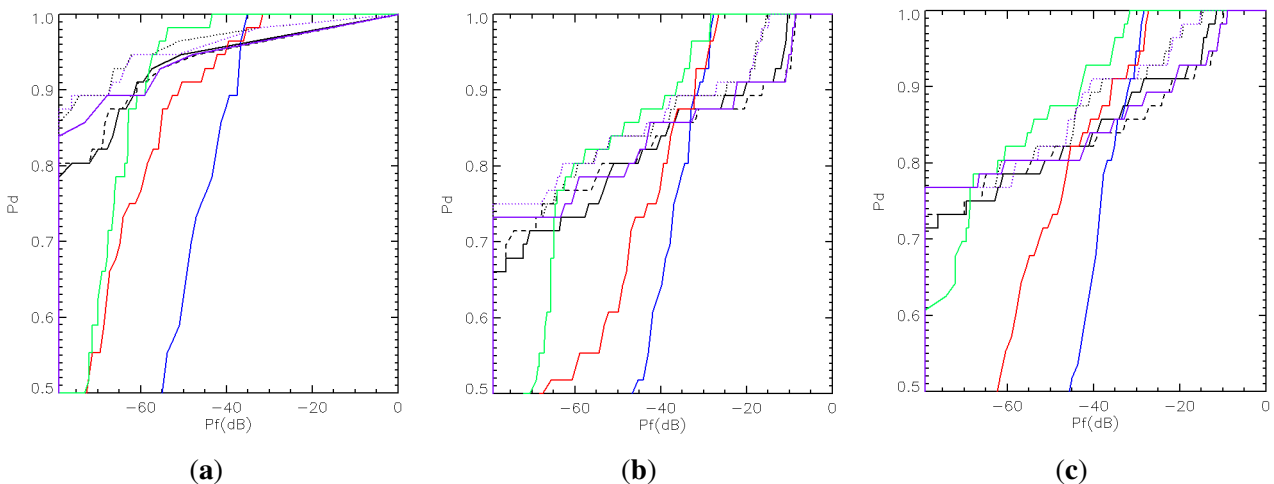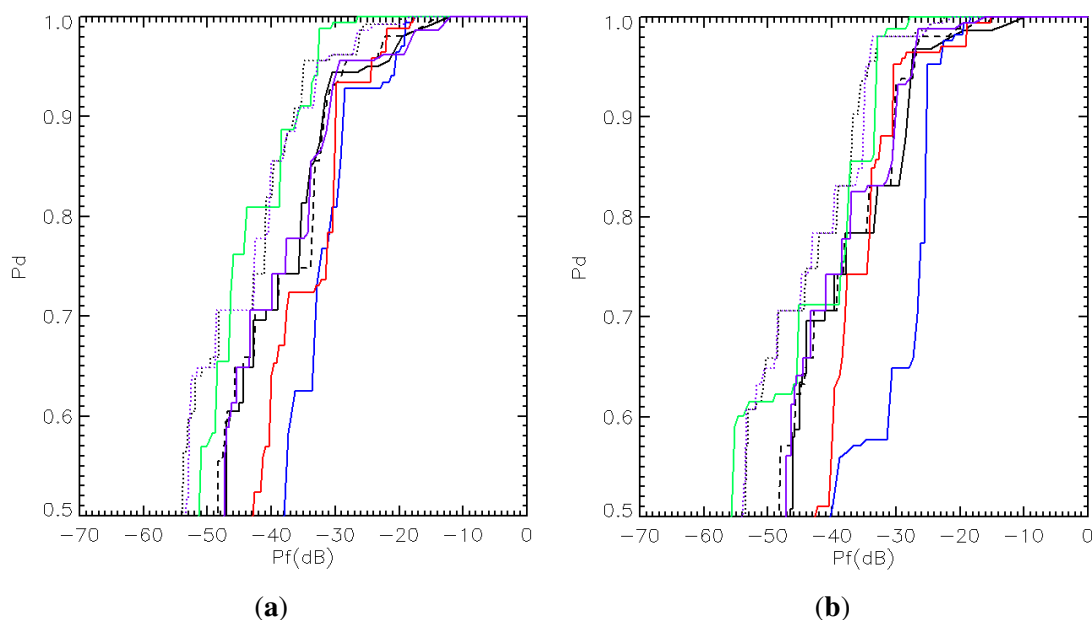

Figure 7. Detector ROC curves for sub-look analysis in the azimuth direction. RADARSAT-2 fine quad-pol data. Boxcar filter: 3×5 (range $\times$ azimuth) pixels. (**a**) HV channel; (**b**) HH channel; (**c**) VV channel. Vessels analyzed: 69; pixels used for P_f: $\sim 10^{-7}$. Black: sub-look correlation (solid: filtered with no overlap; dashed: filtered 30% overlap); blue: sub-look coherence; green: GLRT; violet: intensity (dotted: no average; solid: averaged); red: sub-look entropy.

6.2. Comparison with TerraSAR-X Data

6.2.1. Sub-Look Processing in the Range

Figure 8 presents the ROC curves obtained for the TerraSAR-X dataset using a boxcar window of (7×3) pixels for both co-polarization channels. It can be observed that the HH channel provides slightly better results, especially for the intensity detector. This can be linked to the fact that for a Bragg surface, the power of the VV channel is supposed to be greater than the one of HH. In terms of algorithm comparison, the results are similar to the ones obtained with RADARSAT-2 data. The GLRT provides the best performance, closely followed by the SLC intensity. The sub-look coherence, entropy and correlation methods present ROC curves that are generally lower. However, their performances are rather similar to the corresponding ones in the RADARSAT-2 dataset for high P_d values.

As for the previous datasets, the impact of different averaging is analyzed exploiting a boxcar window of (135×5) pixels. The performance is reduced, in line with the previous findings.

(a)   **(b)**

Figure 8. Detector ROC curves for sub-look analysis in the range. TerraSAR-X HH/VV data. Boxcar filter: 7×3 (range $\times$ azimuth) pixels. (**a**) VV channel; (**b**) HH channel. Vessels analyzed: 49; pixels used for P_f: $\sim 10^{-8}$. Black: sub-look correlation (solid: filtered with no overlap; dashed: filtered 30% overlap); blue: sub-look coherence; green: GLRT; violet: intensity (dotted: no average; solid: averaged); red: sub-look entropy.

### 6.2.2. Sub-Look Processing in Azimuth

The ROC curves for the azimuth analysis are not shown here for the sake of brevity. Once again, they are very similar to the curves for the range analysis, but they depict a slight worsening of the performances, probably due to the ships' movements. Moreover, the azimuth resolution is lower than the range one, and therefore, splitting the spectrum in the azimuth would provide a more significant loss in terms of spatial resolution.

6.3. Comparison with ALOS-PALSAR Data

6.3.1. Sub-Look Processing in the Range

The ROC curves for this dataset are presented in Figure 9, using a boxcar window of (3×15) pixels. Notice that some ROC curves exploiting this dataset were already presented in [43]. In this paper, the training area for false alarms only partially includes the artifacts region, and therefore, this work shows results that are in between the two ROCs presented in [43].
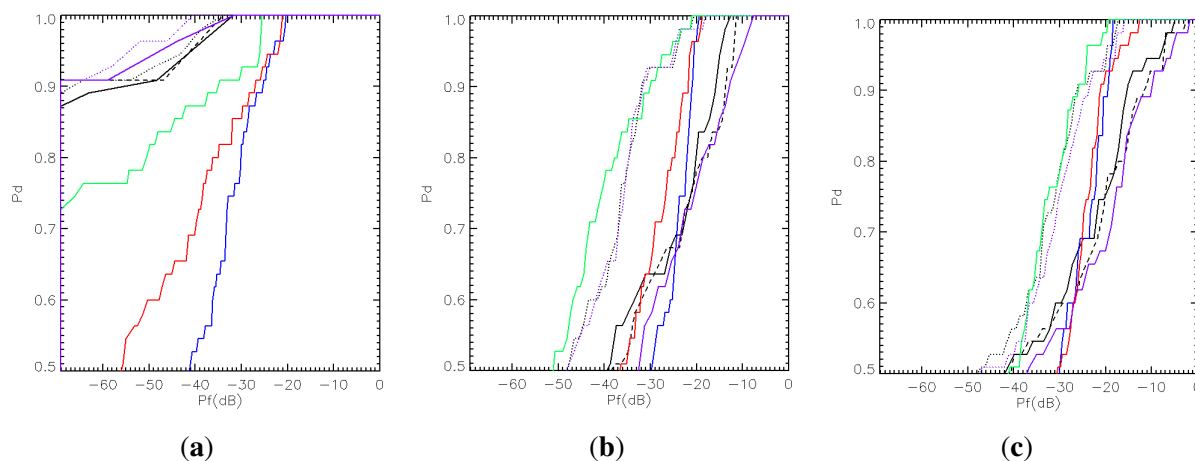
Figure 9. Detector ROC curves for sub-look analysis in the range. ALOS-PALSAR quad-polarimetric data. Boxcar filter: 3×15 (range $\times$ azimuth) pixels. (**a**) HV channel; (**b**) HH channel; (**c**) VV channel. Vessels analyzed: 53; pixels used for P_f: $\sim 10^{-7}$. Black: sub-look correlation (solid: filtered with no overlap; dashed: filtered 30% overlap); blue: sub-look coherence; green: GLRT; violet: intensity (dotted: no average; solid: averaged); red: sub-look entropy.

The obtained results are relatively different from the previous datasets. It can be observed that for the cross-polarization channel, the intensity detector and the sub-look correlation present a higher performance than the other sub-look detectors. However, the results are reversed if the co-polarizations are considered instead, and the order of performance is similar to that of RADARSAT-2 and TerraSAR-X, indicating the importance of polarimetric information for this dataset (i.e., the HV channel yields substantial improvement in ship detection). An explanation for such an excellent performance of the HV intensity detector is that the sea background becomes particularly low in HV, due to the fact that the sea can be well modeled as a Bragg surface (where the cross-channel is zero). In this situation, the improvement provided by the sub-look analysis to minimize P_f is not very significant, since the clutter is already very low. Some further analysis of the relative importance of polarimetric channels can also be found in [50]. On the other hand, the reduction of the resolution associated with the splitting of the spectrum diminishes P_d. The sub-look correlation seems somehow not to be strongly affected by this and provides a performance not much lower than the intensity one. This notwithstanding, it is important to remark that in this dataset, very small vessels were considered. An additional test was performed excluding such very small targets in order to understand if they were the cause for the loss of performance of the sub-look detectors. Without them, all of the detectors obtain better ROC curves,

but the rank of detectors remains unchanged. These ROCs are not shown for the sake of brevity. For the co-polarizations, a different scenario is observed, because their backscattering is fairly high due to the higher sea state and steep incidence angle. Consequently, the use of sub-look analysis once again helps with reducing the clutter level and improving the final performance. Again, the use of a larger window size reduces the performance.

6.3.2. Sub-Look Processing in the Azimuth

The final analysis considers the azimuth processing for ALOS data. The ROC curves are not presented here for the sake of brevity, but they are rather similar to the range ones. However, it appears that some of the detectors experience a slight improvement, opposite of the other datasets. This gain may be due to the much higher resolution of ALOS data in the azimuth. Therefore, performing sub-looks in the azimuth direction is less critical in terms of spatial resolution loss, despite the fact that azimuth processing is affected by the ships movements.

7. Discussions

In the following, some conclusions are drawn regarding different aspects:

- Polarization channels: The images acquired for the comparison consider different polarization channels. RADARSAT-2 and ALOS-PALSAR are both quad polarimetric, while TerraSAR-X is HH/VV dual polarimetric. In the performed test, it seems that the cross-polarization (HV) provides the best ROC curves for all of the experiments. This has been also reported by several researchers [3,40]. Additionally, this result is in line with the assumption that the sea can be modeled as a Bragg surface [9,51], which assumes a null cross-polarization. It has to be considered, as well, that vessels may scatter less in the cross-channel. However, such a reduction is not as large as for the sea, leading to a higher vessel-sea contrast. Certainly, this is mostly evident in situations where sea clutter is strong (as for harsh weather conditions). Regarding the two co-polarization channels (HH and VV), their performance is comparable, but, in some instances, the results for HH seem to be slightly better [45]. Besides the scattering from the sea (which is, on average, stronger in VV compared to HH), this fact may be due to the effect of dihedral scattering (e.g., double-bounce) between sea and vessel, especially if the vessel has one axis oriented along the azimuth direction. Indeed, horizontal dihedral scattering is stronger in the HH channel compared to the VV channel. As a final remark, we could say that the use of the cross-polarization would be preferred, and the importance of sub-look processing will reveal more when the cross-polarization cannot be acquired, because only single-polarimetric data co-polarized channels are available.
- Central frequency and resolution: The possibility of comparing three different SAR systems allows some analysis concerning the frequency providing the best ROC curves. Three frequencies have been exploited, L-, C- and X-band. Clearly, the ROC curves for the different sensors are not utterly comparable, since the images were not acquired at the same time, and the sensors' resolution and incidence angle are different. Therefore, the following conclusions are only indicative. Firstly, the results obtained with RADARSAT-2 and TerraSAR-X are compared, without considering the cross-polarization channel. From the analysis, it seems that RADARSAT-2 and TerraSAR-X

provide similar ROC curves for values of $P_d > 0.8$, and RADARSAT-2 generally has better ROCs for $P_d < 0.8$. Even if TerraSAR-X offers a higher resolution (about 2.5×6.5 m compared with 5.2×10 m of RADARSAT-2), the performance of RADARSAT-2 is as good as the one of TerraSAR-X (or even better for lower values of P_d). An explanation for this could be related to the fact that the sea states captured by the images were particularly high, and sea clutter appears stronger in the X-band. For this reason, if the spatial resolution were the same, the C-band could be advantageous when weather conditions are expected to be rough. Secondly, the ALOS dataset shows a detection performance comparable to the one of RADARSAT-2 in the cross-polarization. Following the previous rationale, the L-band should provide an even lower sea clutter. On the contrary, vessels at the L-band may have a lower backscattering, as well (unless they are very large), and the resolution of ALOS is poorer than RADARSAT-2. These two drawbacks may be causing the lower performance of ALOS at the co-polarization channels.

- Comparison with the intensity detector: The intensity detector is tested in order to understand if the sub-look analysis provides noticeable benefits. In general, such sub-look analysis requires images in the SLC format and not detected by multi-look. In this work, the intensity detector has been also used as a reference for the other algorithms, since it is a well-known and standard method. Looking at the obtained results, the ROC curves clearly show that the sub-look analysis generally provides an improved performance. However, such enhancement is in some situations very small, as for the ALOS cross-polarization. It can be also observed that the main advantages of the sub-look analysis are more evident when the co-polarizations are used and the clutter is stronger. *Per contra*, in situations where the clutter contribution is low, a simple threshold on the cross-polarization backscattering may be satisfactory.

- Best detector: For our analyses (with the exception of the ALOS cross-polarization), the GLRT detector provides the best ROC curves, even though the improvement on TerraSAR-X data is not very large. The GLRT is the only sub-look detector that does not require spatial averaging (i.e., it works on single pixels), and that is the most likely reason for the better performance. The only loss of resolution experienced by this detector is because of the spectrum splitting (i.e., the generation of the sub-images), which corresponds to 50% in these experiments.

- Dimensions of averaging windows: Speckle filtering is another source of resolution loss, and therefore, it is valuable to consider its effect on the performance. In this work, the boxcar windows are always rectangular and not squared, in order to finally obtain areas on the ground that are approximately squared. For the intensity detector, it can be observed that omitting speckle filtering provides better ROC curves. Therefore, the loss of resolution due to the spatial averaging is not compensated by the reduction of speckle variation. Similarly, if the averaging window of the sub-look coherence or entropy detectors is reduced, their performances improve, even if not very largely. Nevertheless, there is a threshold value for the averaging window size when the performance is optimized and any smaller window returns worse results. In the limit, a window of (1×1) pixels produces always $P_d = P_f = 1$. The reason for this result is that the estimation of these detectors' outputs is more critical than the one of the intensity detector, and the use of a few pixels provides strongly biased results. Therefore, this counterbalances the improvement of having higher resolution. Likewise, the sub-look correlation has an optimal dimension of the

averaging window, but when the window is reduced to (1×1) pixels, the obtained ROC becomes very similar to the one of the SLC (unfiltered) intensity. The explanation for this is because the product of the two sub-looks is not completely canceling the sea clutter out, since this may happen only after averaging (the output has the same information content as the intensity image, except for a loss of resolution due to the spectrum splitting and the absence of a square). As a final remark regarding the exploitation of small averaging windows, a minor speckle reduction may have some disadvantages when a statistical test is exploited for setting the detection threshold. This rationale is mostly true if the pdf is well-known. A reduction of variance may have the opposite effect of having a test that sets the threshold very close to the mean, neglecting heavier tails and providing, then, more false alarms than expected.

8. Conclusions

Ship detection using SAR data is a relevant application of remote sensing, and as a result, several methodologies have been proposed in the last few decades.

The work carried out in this paper can be summarized as follows. This paper focused on algorithms exploiting spectral (or sub-look) analysis (i.e., Fourier transform of the complex SAR image). Targets that present stability in the spectral domain are often referred to as coherent targets. In the context of ship detection, sub-look analysis is based on the idea that portions of the sea clutter SLC spectrum are uncorrelated, while vessels usually preserve high correlation along the spectrum. In this work, several sub-look algorithms have been tested employing several SAR images, accompanied by reference information, such as AIS vessel location and wind speed. For ensuring and maximizing the benefits of the sub-look analysis, situations where sea clutter is strong (as in harsh weather conditions) have been considered. Additionally, the selected datasets bring diversity in frequency, polarization and incidence angles in order to provide some statistics that can cover a variety of scenarios. In particular, the employed data consider three sensors: RADARSAT-2, TerraSAR-X and ALOS-PALSAR. The selected criterion for the detectors comparison is the estimation of ROC curves, which provides information independent of the specific threshold selection. Since some of the algorithms exploit averaging to estimate their outputs, several tests have been carried out to investigate the performance dependency on the window size.

The two main novelties of this work are:

- Initially, two algorithms previously used for the detection of coherent targets on land and natural areas were tested for the first time ever on ship detection. These approaches are the GLRT and the sub-look entropy [6,33]. The sub-look entropy detector allows one to split the spectrum into several sections (also with large overlap), providing that vessels that are not stable in a few sections can still be detected. The GLRT detector, in addition, does not require spatial averaging (apart from the initial sub-looking), and therefore, the resolution is only slightly reduced.

- Secondly, there are no similar studies that compare the same amount of sub-look ship detectors over such a large and variable dataset. The main idea behind this study is to understand if sub-look analysis provides benefits compared with ordinary backscattering analysis. In other words, the benefits of acquiring and exploiting the phase of the SAR image compared to only the detected images is investigated.

The most important finding of the work is that the sub-look analysis seems to provide some overall benefits when the detection task is more challenging (e.g., the intensity contrast between target and sea is small). However, if the contrast is large (as for the cross-polarization in the L-band), an algorithm setting a threshold on the intensity image can provide very comparable results with a faster implementation. Therefore, the sub-look detectors should be used as complementary to the intensity detectors to help with increasing the contrast between ships and sea when this is low.

As future work, the possibility of combining polarimetric information in a common framework with the sub-look analysis will be analyzed and tested.

Acknowledgments

Author Contributions

Armando Marino contributed in the acquisition of TerraSAR-X and RADARSAT-2 data, comparison of algorithms, interpretation of the results and writing of the manuscript. *Maria J. Sanjuan-Ferrer* contributed in the design of the GLRT algorithm and writing of the manuscript. *Irena Hajnsek* contributed in the acquisition of TerraSAR-X data, interpretation of the results and preparation of the manuscript. *Kazuo Ouchi* contributed in the acquisition of ALOS data and the preparation of the manuscript.

Conflicts of Interest

The authors declare no conflict of interest.

References

1. Barele, V.; Gade, M. *Remote Sensing of the European Seas*; Springer: Berlin, Germany, 2008.
2. Franceschetti, G.; Lanari, R. *Synthetic Aperture Radar Processing*; CRC Press: Boca Raton, FL, USA, 1999.
3. Crisp, D.J. The State-of-the-Art in ship detection in Synthetic Aperture Radar imagery. Available online: http://oai.dtic.mil/oai/oai?verb=getRecord&metadataPrefix=html&identifier=ADA426096 (accessed on 9 April 2015).
4. Sanjuan-Ferrer, M.J. Detection of Coherent Scatterers in SAR Data: Algorithms and Applications. Ph.D. Thesis, ETH Zurich, Zurich, Switzerland, 2013.

5. Sanjuan-Ferrer, M.; Hajnsek, I.; Papathanassiou, K.; Moreira, A. A new detection algorithm for coherent scatterers in SAR data. *IEEE Trans. Geosci. Remote Sens.* **2015**, submitted.

6. Schneider, R.Z.; Papathanassiou, K.P.; Hajnsek, I.; Moreira, A. Polarimetric and interferometric characterization of coherent scatterers in urban areas. *IEEE Trans. Geosci. Remote Sens.* **2006**, *44*, 971–984.

7. Arnaud, A. Ship detection by SAR interferometry. In Proceedings of the IEEE 1999 International Geoscience and Remote Sensing Symposium, Hamburg, Germany, 28 June–2 July 1999; Volume 5, pp. 2616–2618.

8. Ouchi, K.; Tamaki, S.; Yaguchi, H.; Iehara, M. Ship detection based on coherence images derived from cross correlation of multilook SAR images. *IEEE Geosci. Remote Sens. Lett.* **2004**, *1*, 184–187.

9. Jackson, C.R.; Apel, J.R. *Synthetic Aperture Radar Marine Users Manual*; U.S. DEPARTMENT OF COMMERCE, National Oceanic and Atmospheric Administration (NOAA). Avasilable online: http://www.sarusersmanual.com/ (accessed on 23 April 2015).

10. Cloude, S.R. *Polarisation: Applications in Remote Sensing*; Oxford University Press: Oxford, UK, 2009.

11. Alpers, W. *Imaging Ocean Surface Waves by Synthetic Aperture Radar: A Review*; Ellis Horwood Ltd.: Cambridge, UK, 1983.

12. Elfouhaily, T.B.; Chapron, K.K.; Vandemark, D. A unified directional spectrum for long and short wind-driven waves. *J. Geophys. Res.* **1997**, *102*, 15781–15796.

13. Plant, W.J. *Surfaces, Waves and Fluxes: Bragg Scattering of Electromagnetic Waves from the Air/Sea Interface*; Kluwer Academic: Dordrecht, The Netherlands, 1990.

14. Thompson, D.R. *Radar Scattering from Modulated Wind Waves: Calculation of Microwave Doppler Spectra from the Ocean Surface with a Time-Dependent Composite Model*; Kluwer Academic: Dordrecht, The Netherlands, 1989.

15. Wackerman, C.; Friedman, K.; Pichel, W.; Clemente-Colon, P.; Li, X. Automatic detection of ships in RADARSAT-1 SAR imagery. *Can. J. Remote Sens.* **2001**, *27*, 568–577.

16. Brizi, M.; Lombardo, P.; Pastina, D. Exploiting the shadow information to increase the target detection performance in SAR images. In Proceedings of the 5th International Conference on Radar Systems, RADAR'99: Brest, Germany, 17–21 May 1999.

17. Campbell, J.; Vachon, P. Optimisation of the Ocean FeaturesWorkstation for ship detection. Canadian Centre of Remote Sensing: Suwanee, GA, USA, 1997.

18. Marino, A.; Cloude, S.R.; Woodhouse, I.H. A polarimetric target detector using the Huynen Fork. *IEEE Trans. Geosci. Remote Sens.* **2010**, *48*, 2357–2366.

19. Chapple, P.; Bertilone, D.; Caprari, R.; Newsam, G. Stochastic modelbased processing for detection of small targets in non-Gaussian natural imagery. *IEEE Trans. Image Process.* **2001**, *10*, 554–564.

20. Conte, E.; Lops, M.; Ricci, G. Asymptotically optimum radar detection in compound-Gaussian clutter. *IEEE Trans. Aerospace Electron. Syst.* **1995**, *31*, 617–625.

21. Ferrara, G.; Migliaccio, M.; Nunziata, F. and Sorrentino, A. Generalized-K (GK)-based observation of metallic objects at sea in full-resolution Synthetic Aperture Radar (SAR) data: a multipolarization study. *IEEE J. Ocean. Eng.* **2011**, *36*, 195–204.

22. Friedman, K.; Wackerman, C.; Funk.; Pichel, W.; Clemente-Colon, P.; Li, X. Validation of a CFAR vessel detection algorithm using known vessel locations. In Proceedings of the 2001 IEEE International Geoscience and Remote Sensing Symposium (IGARSS'01), Sydney, NSW, Australia, 9–13 July 2001; pp. 1804–1806.

23. Johannessen, J. Coastal observing systems: The role of synthetic aperture radar. *Johns Hopkins APL Tech. Dig.* **2000**, *21*, 41–48.

24. Lopes, A.; Nezry, E.; Touzi, R.; Laur, H. Structure detection and statistical adaptive speckle filtering in SAR images. *Int. J. Remote Sens.* **1993**, *14*, 1735–1758.

25. Olsen, R.; Wahl, T. The ship detection capability of ENVISAT's ASAR. In Proceedings of the IEEE 2003 International Geoscience and Remote Sensing Symposium (IGARSS'03), Toulouse, France, 21–25 July 2003.

26. Schwartz, G.; Alvarez, M.; Varfis, A.; Kourti, N. Elimination of false positives in vessels detection and identification by remote sensing. In Proceedings of the 2002 IEEE International Geoscience and Remote Sensing Symposium (IGARSS-02), Toronto, ON, Canada, 24–28 June 2002; pp. 116–118.

27. Wang, C.; Jiang, S.; Zhang, H.; Wu, F.; Zhang, B. Ship detection for high-resolution SAR images based on feature analysis member. *IEEE Geosci. Remote Sens. Lett.* **2014**, *11*, 119–123.

28. Brusch, S.; Lehner, S.; Fritz, T.; Soccorsi, M.; Soloviev, A.; van Schie, B. Ship surveillance with TerraSAR-X. *IEEE Trans. Geosci. Remote Sens.* **2011**, *49*, 1092–1103.

29. Iervolino, P.; Guida, R.; Whittaker, P. NovaSAR-S and maritime surveillance. In Proceedings of the 2013 IEEE Geoscience and Remote Sensing Symposium, Melbourne, Australia, 21–26 July 2013.

30. Dell Acqua, F.; Gamba, P.; Lisini, G. Rapid mapping of high resolution SAR scenes. *ISPRS J. Photogramm. Remote Sens.* **2009**, *62*, 482–489.

31. Kay, S.M. *Fundamentals of Statistical Signal Processing*; Prentice Hall: Upper Saddle River, NJ, USA, 1993.

32. Riley, K.F.; Hobson, M.P.; Bence, S.J. *Mathematical Methods for Physics and Engineering*; Cambridge University Press: Cambridge, UK, 2006.

33. Sanjuan-Ferrer, M.J.; Hajnsek, I.; Papathanassiou, K.P. Analysis of the detection performance of Coherent Scatterers in SAR images. In Proceedings of the 2012 IEEE International Geoscience and Remote Sensing Symposium (IGARSS), Munich, Germany, 22–27 July 2012.

34. Souyris, J.C.; Henry, C.; Adragna, F. On the use of complex SAR image spectral analysis for target detection: Assessment of polarimetry. *IEEE Trans. Geosci. Remote Sens.* **2003**, *41*, 2725–2734.

35. Brekke, C.; Anfinsen, S.N.; Larsen, Y. Subband extraction strategies in ship detection with the subaperture cross-correlation magnitude. *IEEE Geosci. Remote Sens. Lett.* **2013**, *10*, 786–790.

36. Oliver, C.; Quegan, S. *Understanding Synthetic Aperture Radar Images*; SciTech Publishing, Inc.: Herndon, VI, USA, 2004.

37. Cumming, I.; Wong, F. *Digital Processing of Synthetic Aperture Radar Data: Algorithms and Implementations*; Artech House: Boston, MA, USA, 2005.

38. Ouchi, K.; Iehara, M.; Morimura, K.; Kumano, S.; Takami, I. Nonuniform azimuth image shift observed in the Radarsat images of ships in motion. *IEEE Trans. Geosci. Remote Sens.* **2002**, *40*, 2188–2195.

39. Anfinsen, S.N.; Brekke, C. Statistical models for constant false alarm rate ship detection with the sublook correlation magnitude. In Proceedings of 2012 IEEE International Geoscience and Remote Sensing Symposium (IGARSS), Munich, Germany, 22–27 July 2012; pp. 5626–5629.

40. Touzi, R. On the use of polarimetric SAR data for ship detection. In Proceedings of the 1999 IEEE International Geoscience and Remote Sensing Symposium, Hamburg, Germany, 28 June–2 July 1999; pp. 812–814.

41. Yeremy, M.; Geling, G.; Rey, M.; Plache, B.; Henschel, M. Results from the CRUSADE ship detection trial: Polarimetric SAR. In Proceedings of the 2002 IEEE International Geoscience and Remote Sensing Symposium, Toronto, ON, Canada, 24–28 June 2002 .

42. Marino, A. A notch filter for ship detection with polarimetric SAR data. *IEEE J. Sel. Top. Appl. Earth Obs. Remote Sens.* **2013**, *6*, 1219–1232.

43. Marino, A.; Sugimoto, M.; Ouchi, K.; Hajnsek, I. Validating a notch filter for detection of targets at sea with ALOS-PALSAR data: Tokyo bay. *IEEE J. Sel. Top. Appl. Earth Obs. Remote Sens.* **2013**, *7*, 4907–4918 .

44. Marino, A.; Walker, N. Ship detection with quad polarimetric TerraSAR-X data: An adaptive notch filter. In Proceeding of the 2011 IEEE International Geoscience and Remote Sensing Symposium (IGARSS), Vancouver, BC, USA, 24–29 July 2011 ; pp. 245–248.

45. Migliaccio, M.; Nunziata, N.; Montuori, A.; Paes, R. L. Single Look Complex COSMO-SkyMed SAR data to observe metallic targets at sea. *IEEE J. Sel. Top. Appl. Earth Obs. Remote Sens.* **2012**, *5*, 893–901.

46. Nunziata, F.; Migliaccio, M.; Brown, C. Reflection symmetry for polarimetric observation of man-made metallic targets at sea. *IEEE J. Ocean. Eng.* **2012**, *37*, 384–394.

47. Velotto, D.; Nunziata, F.; Migliaccio, M.; Lehner, S. Dual-Polarimetric TerraSAR-X SAR data for target at sea observation. *IEEE Geosci. Remote Sens. Lett.* **2013**, *10*, 1114–1118.

48. Cameron, W.; Youssef, N.; Leung, L. Simulated polarimetric signatures of primitive geometrical shapes. *IEEE Trans. Geosci. Remote Sens.* **1996**, *34*, 793–803.

49. Tomiyasu, K. and Scheiber, R. Detecting weak targets in a speckled distributed scene by SAR reconfiguration. In Proceedings of the 2009 IEEE Radar Conference (RadarCon), Pasadena, CA, USA, 4–8 May 2009.

50. Sugimoto, M.; Ouchi, K.; Nakamura, Y. On the similarity between dual- and quad-eigenvalue analysis in SAR polarimetry. *Remote Sens. Lett.* **2013**, *4*, 956–964.

51. Elachi, C.; van Zyl, J. *Introduction To The Physics and Techniques of Remote Sensing*; John Wiley and Sons: Hoboken, NJ, USA, 2006.